International Forum on Aeroelasticity and Structural Dynamics
IFASD 2017
25-28 June 2017 Como, Italy

APPLICATION OF UNSTEADY AERODYNAMIC REDUCED-ORDER MODELING TECHNIQUES TO A COMPLEX CONFIGURATION

Maximilian Winter[1] **and Christian Breitsamter**[1]

[1]Technical University of Munich
Department of Mechanical Engineering
Chair of Aerodynamics and Fluid Mechanics
Boltzmannstr. 15, 85748 Garching, Germany
maximilian.winter@aer.mw.tum.de
christian.breitsamter@aer.mw.tum.de

Keywords: Reduced-order modeling, Unsteady aerodynamics, Complex configuration, CRM

Abstract: In the present work, different nonlinear reduced-order modeling (ROM) approaches are employed to assess their performance and efficiency for unsteady aerodynamic computations. The ROM techniques are applied to a complex aircraft model in order to indicate their potential for industrial applications. On the one hand, a neurofuzzy-model-based ROM is employed to compute the aerodynamic response due to small-amplitude motions across variable angles of attack. On the other hand, the unsteady surface pressure distribution is predicted by combining system identification methods with the proper orthogonal decomposition (POD). For demonstrations purposes, NASA's common research model (CRM) configuration is investigated at transonic flow conditions, while forced-motion computational fluid dynamics (CFD) simulations are carried out to obtain the aerodynamic responses induced by structural mode-shape-based deflections. It is shown that the presented methods can be applied to speed-up multidisciplinary analyses with respect to industry-relevant configurations.

1 INTRODUCTION

In recent years, a lot of effort has been invested in the development of ROMs to accelerate unsteady aerodynamic and aeroelastic analyses. This progress is driven by the need to incorporate the fidelity of CFD approaches into multidisciplinary simulation frameworks. It is unquestionable that the CFD-based aerodynamic modeling significantly enhances the accuracy of aeroelastic predictions at transonic flow conditions in comparison to potential-flow-theory-based methods. However, the advantage in fidelity comes along with a drastically increased computational effort. As a possible remedy, ROMs have been developed and applied to overcome this limitation. The general functionality of system-identification-based ROMs, which are in the focus of this investigation, is the exploitation of CFD-generated training data in order to obtain a black-box model of the physical system under investigation. In the context of aeroelastic computations, the system inputs are the structural and rigid body degrees of freedom, whereas the outputs are represented by the motion-induced generalized aerodynamic forces [1,2]. The application of the ROM with respect to the production simulations is far more efficient than solving the full-order CFD equations. In this way, a significant speed-up can be achieved. Below, a brief overview of selected identification-based ROM approaches in the context of unsteady aerodynamic and aeroelastic applications is given.

Dowell and Hall [3] and Lucia et al. [4] recapitulated several established ROM concepts. Specifically, approaches based on the Volterra theory [5,6] and the POD [7,8] are discussed. Moreover, numerous methods developed within the system identification and control community have been adopted for aerospace applications, e.g., the eigensystem realization algorithm (ERA) [9–12] and the auto-regressive moving average (ARMA) model [13]. Under the assumption that the system's response is linearly related to the respective inputs, the aforementioned identification techniques are well-suited to obtain a black-box model of the underlying aerodynamic system. For the prediction of large amplitude motions (inducing aerodynamic nonlinearities) or nonlinear parameter influences such as varying freestream conditions, however, nonlinear system identification strategies must be developed and employed. In this regard, the use of multilayer-perceptron (MLP) neural networks has been proposed by Faller and Schreck [14], Voitcu and Wong [15] as well as Mannarino and Mantegazza [16], whereas radial basis function (RBF) neural networks were successfully employed by Zhang et al. [17] and Winter and Breitsamter [18]. Moreover, some recently developed nonlinear identification techniques yielded promising results for unsteady aerodynamic reduced-order modeling tasks [1, 19, 20]. Besides, the combination of identification-based approaches with the POD has been investigated by Park et al. [21], Lindhorst et al. [22, 23], and Winter and Breitsamter [2] in order to model surface or field quantities of the flow. ROMs that are able to deal with nonlinear parameter variations, i.e., the Kriging-interpolation-based approaches of Glaz at al. [24] and Liu et al. [25] as well as the neurofuzzy-model-based methodologies of Winter and Breitsamter [1, 26], have been shown to be suited for efficient and accurate aerodynamic computations across varying freestream conditions. Nonetheless, most of the previously outlined research focuses on the introduction of novel approaches, whereas the application is demonstrated by means of a low-complexity test case. In contrast, the aim of this work is the application of recently developed ROM approaches towards a more realistic aircraft configuration.

In the present work, two ROM approaches originating from the Chair of Aerodynamics and Fluid Mechanics of the Technical University of Munich (TUM-AER) are applied to assess their performance and efficiency with respect to a complex configuration. On the one hand, the neurofuzzy-model-based ROM robust to varying freestream conditions [1, 26] is employed. In this way, the aerodynamic response due to small-amplitude motions is modeled across different angles of attack with a single ROM. The resulting aerodynamic dataset can be utilized for classical aeroelastic stability considerations, i.e., flutter onset estimation. On the other hand, the unsteady surface pressure distribution is predicted by combining system identification methods with the POD, see [2] for instance. The second ROM approach is well-suited for the efficient computation of the steady and unsteady air load distribution. For demonstration purposes, NASA's CRM configuration [27, 28] is considered at transonic flow conditions. In order to obtain the training data, forced-motion CFD computations are carried out yielding the aerodynamic responses induced by structural-eigenmode-based deflections. Therefore, the mode shapes from the FERMAT configuration [29] are adopted. Subsequently, the ROMs are conditioned, tested, and evaluated. Concerning the latter task, a comparison with the full-order CFD solution is presented for performance and efficiency classification.

2 THEORY AND COMPUTATIONAL METHODS

2.1 Aeroelastic Simulation Framework

Computational models of aircraft structures are commonly obtained by means of the finite-element method (FEM), [30]. As complex structures may involve a large number of elements and, consequently, many degrees of freedom, the models constructed in physical space are usually transferred into generalized coordinates to reduce the computational costs. According to [1], the well-known equations of motion for a multi-modal structural system can be written as

$$\mathbf{M}_{gen}\ddot{\mathbf{q}}(t) + \mathbf{C}_{gen}\dot{\mathbf{q}}(t) + \mathbf{K}_{gen}\mathbf{q}(t) = q_\infty l_{ref}^3 \cdot \mathbf{f}_{gen}(t) \quad \text{with} \;\; \mathbf{f}_{gen}(t) = \mathbf{\Phi}^T\mathbf{f}(t). \tag{1}$$

A modal analysis provides the respective generalized mass, damping, and stiffness matrices, $\mathbf{M}_{gen}$, $\mathbf{C}_{gen}$, and $\mathbf{K}_{gen}$, as well as the modal matrix $\mathbf{\Phi} = [\boldsymbol{\phi}_1, \boldsymbol{\phi}_2, \ldots, \boldsymbol{\phi}_N]$. In Eq. 1, $\mathbf{q}(t) \in \mathbb{R}^N$ denotes the modal or generalized coordinates with N being the number of considered eigenmodes. Since the CFD computations are performed using nondimensional quantities in this context, the generalized aerodynamic forces $\mathbf{f}_{gen}$ are considered as normalized by $q_\infty l_{ref}^3$. Taking only pressure-based aerodynamic loads into account, the ith generalized force vector element can be expressed as

$$f_{gen,i}(t) = \int_{\mathbf{S}} c_p(t)\ \boldsymbol{\phi}_i \cdot d\mathbf{S}. \tag{2}$$

Considering Eq. 2, the local pressure coefficient c_p is integrated over the surface $\mathbf{S}$ and weighted with the ith mode shape $\boldsymbol{\phi}_i$. By assuming a linear relation between the structural excitation and the unsteady air loads, the well-known linear frequency domain flutter equation can be obtained:

$$\Big[-\omega^2\mathbf{M}_{gen} + i\omega\mathbf{C}_{gen} + \mathbf{K}_{gen} - q_\infty l_{ref}^3 \cdot \mathbf{GAF}(ik_{red}) \Big] \cdot \mathbf{q}_0 = \mathbf{0} \tag{3}$$

Equation 3 introduces the angular frequency ω, the reduced frequency $k_{red} = (\omega \cdot c_{ref})/U_\infty$ and the complex-valued $\mathbf{GAF} \in \mathbb{C}^{N\times N}$ matrix representing the linear aerodynamic transfer function in the frequency domain. Since the $\mathbf{GAF}$ matrix can be computed by both the CFD solver and the neurofuzzy ROM approach [1], the datasets are suited for comparison and verification purposes.

2.2 Computational Fluid Dynamics Solver – AER-Eu

In the course of this investigation, the inviscid CFD solver AER-Eu is employed to compute the training data needed for ROM construction. Besides, AER-Eu is used to generate the reference solution for the application tests in order to evaluate the accuracy of the ROM approaches. The CFD code AER-Eu developed at TUM-AER solves the Euler equations in conservation form by utilizing a shock-capturing finite-volume method based on multi-block-structured grids [31]. Therefore, Roe's flux-difference splitting is utilized for the spatial discretization, whereas the

monotonic-upstream-scheme-for-conservation-laws (MUSCL) extrapolation is used for retaining the total variation diminishing property. The temporal integration is carried out with Jameson's implicit dual-time-stepping scheme, while the embedded pseudo-time iterations are computed by means of the lower-upper symmetric successive over-relaxation. Furthermore, several deforming mesh approaches have been implemented. For example, a user-defined time law can be specified to interpolate between a reference grid and various amplitude grids. Further information about the CFD solver framework can be found in Refs. [11, 31–34].

2.3 Nonlinear System Identification

In general, identification methods are used to obtain a model by processing a set of known input/output data that are representative for the underlying system. For this purpose, a well-known approach is to approximate the dynamic system via a function of current and previous inputs in combination with time-delayed system outputs [35]. In the literature, this principle is referred to as the external dynamics approach or recurrence framework. Here, the system input is the generalized coordinate vector $\mathbf{q}$, while the outputs $\mathbf{y}$ can be represented either by the generalized aerodynamic forces $\mathbf{f}_{gen}$ or the POD coefficients $\mathbf{b}$, [1, 2]. Moreover, a static parameter θ can be included to account for varying freestream conditions, e.g., different incidence angles α_0. With k being the current discrete time increment ($t_{k+1} = t_k + \Delta t$), the external dynamic filter can be generalized to:

$$\tilde{\mathbf{y}}(k) = \mathcal{N}\left[\left(\theta, \mathbf{q}^T(k), \ldots, \mathbf{q}^T(k-m), \mathbf{y}^T(k-1), \ldots, \mathbf{y}^T(k-n)\right)\right] = \mathcal{N}\left[\mathbf{u}_i^T\right] \tag{4}$$

In this way, the identification problem is essentially reduced to a static function approximation task accompanied by the determination of the dynamic delay-orders $m \in \mathbb{N}$ and $n \in \mathbb{N},\ n > 0$ for the respective inputs and outputs; see also [2,35] for instance. As the unknown function $\mathcal{N}$ is expected to be nonlinear for the cases under investigation, neural-network-based methodologies are employed to approximate this functional relationship on the basis of given training data. In the present work, the local linear neuro-fuzzy model developed by Nelles [35] is applied for that purpose. The mathematical framework of a neuro-fuzzy model with N_{LLM} local linear models can be written as:

$$\tilde{f}_i = \sum_{j=1}^{N_{LLM}} \left[w_{j0,i} + w_{j1,i} \cdot (u_{1,i} - c_{j1,i}) + \ldots + w_{jp,i} \cdot (u_{p,i} - c_{jp,i})\right] \cdot \Psi_{j,i}(\mathbf{u}_i) \tag{5}$$

$$\Psi_{j,i}(\mathbf{u}_i) = \frac{\exp\left[-\frac{1}{2}\left(\frac{(u_{1,i}-c_{j1,i})^2}{\sigma_{j1,i}^2} + \ldots + \frac{(u_{p,i}-c_{jp,i})^2}{\sigma_{jp,i}^2}\right)\right]}{\sum_{k=1}^{N_{LLM}} \exp\left[-\frac{1}{2}\left(\frac{(u_{1,i}-c_{k1,i})^2}{\sigma_{k1,i}^2} + \ldots + \frac{(u_{p,i}-c_{kp,i})^2}{\sigma_{kp,i}^2}\right)\right]} \tag{6}$$

In Eqs. 5-6, $u_{l,i}$ symbolizes the lth element of the model input vector related to output $\tilde{f}_i$, whereas the coefficients $w_{jl,i}$ denote the linear model parameters. Besides, $\Psi_{j,i}$ represents the fuzzy validity function that depends on the centers $c_{jl,i}$ and the basis function widths $\sigma_{jl,i}$. Consequently, the validity functions realize a weighting of the respective local linear models

based on the model input regime. In order to obtain the a priori unknown model parameters, the training data are exploited using the local linear model tree (LOLIMOT) algorithm [35]. As a detailed review of the LOLIMOT training procedure is beyond the scope of this work, the reader is referred to the work of Nelles [35] and Winter and Breitsamter [1, 2] for further information.

2.4 Proper Orthogonal Decomposition

The POD snapshot approach originally proposed by Sirovich [36] can be employed to approximate multi-dimensional data by means of a comparatively small set of POD modes; see also Iuliano and Quagliarella [8], Lindhorst et al. [22], and Winter and Breitsamter [2] for instance. In terms of the applications in this work, the snapshot vector $\mathbf{W}_i$ is composed of the pressure coefficients c_p for all CFD surface elements, while subscript i denotes the considered time step. Based on an unsteady simulation involving N_{Trn} training samples, the snapshot matrix $\mathbf{Y}$ can be expressed as:

$$\mathbf{Y} = \left[\hat{\mathbf{W}}_1, \hat{\mathbf{W}}_2, \ldots, \hat{\mathbf{W}}_{N_{Trn}}\right], \qquad \hat{\mathbf{W}}_i = \mathbf{W}_i - \mathbf{A}, \qquad \mathbf{A} = \frac{1}{N_{Trn}} \sum_{i=1}^{N_{Trn}} \mathbf{W}_i \tag{7}$$

Given the snapshot matrix, the objective of the POD is to obtain $M \ll N_{Trn}$ basis vectors that approximate $\mathbf{Y}$ optimal in the least-squares sense. For that purpose, the singular value decomposition (SVD) of $\mathbf{Y}$ is computed; see Eq. 8.

$$\mathbf{Y} = \mathbf{U}\boldsymbol{\Sigma}\mathbf{V}^T = \mathbf{U} \begin{bmatrix} \sigma_1 & \cdots & 0 \\ \vdots & \ddots & \vdots \\ 0 & \cdots & \sigma_{N_{Trn}} \\ 0 & \cdots & 0 \end{bmatrix} \mathbf{V}^T \tag{8}$$

Hence, the first N_{Trn} column vectors of $\mathbf{U}$ result to be the full set of possible POD modes. As the influence of the higher-order POD modes becomes small for practical applications [8], the modes $M+1, \ldots, N_{Trn}$ are not taken into account yielding a reduction of the degrees of freedom for the underlying problem. With respect to the specification of the number of dominant modes M, the relative information content (RIC) criterion is employed [2,8]. Consequently, the resulting POD modes $\boldsymbol{\varphi}$ are taken as a subset of matrix $\mathbf{U}$ (first M column vectors). According to Eq. 9, the full-order system can be approximated utilizing the computed POD modes.

$$\mathbf{W}(t) \cong \mathbf{A} + \sum_{i=1}^{M} b_i(t)\, \boldsymbol{\varphi}_i \tag{9}$$

Nonetheless, prior to ROM construction the coefficients $b_i(t)$ associated to POD mode i have to be determined based on the training data. Therefore, a least-squares solution is computed to obtain the matrix of POD coefficients $\mathbf{B} = [\mathbf{b}(t_1), \mathbf{b}(t_2), \ldots, \mathbf{b}(t_{N_{Trn}})]$. Thus, the system inputs (structural excitations) connected with the corresponding POD coefficient time series can be exploited to generate a model via the system identification approaches outlined in the previous subsection.

3 UNSTEADY AERODYNAMIC REDUCED-ORDER MODELS

Supported by the schematic overviews presented in Figs. 1 and 2, the aerodynamic ROM methodologies proposed in [1] and [2] are briefly recapitulated. As both approaches are based on system identification methods, a set of training data has to be initially provided to construct the ROMs. In this regard, the training data must be representative for the intended use of the models, i.e., the range of amplitudes and frequencies that is of primary interest has to be excited during the training simulations. Hence, adequate signals for structural excitation have to be specified by the user; see [1, 12, 35] for further information.

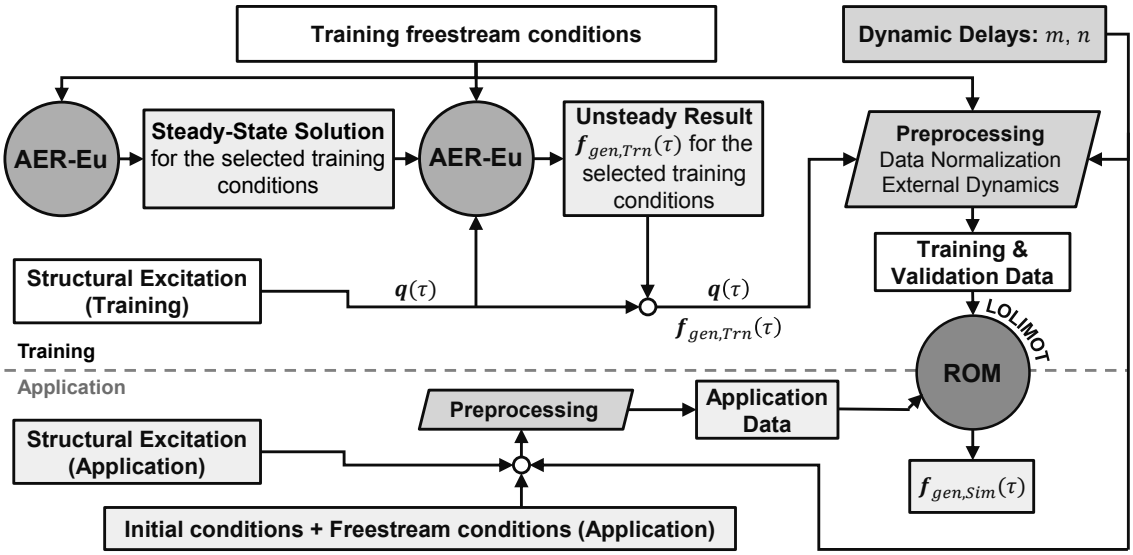

Figure 1: Schematic of the unsteady aerodynamic ROM approach robust to varying freestream conditions.

Based on a priori conducted steady simulations, unsteady forced-motion CFD computations are carried out for the freestream conditions under consideration; see also Figs. 1 and 2. Therefore, the selected training signals are assigned for the excitation of each degree of freedom. Hence, the body shape is given by the superposition of the reference grid and the eigenmode-based deflected grids weighted by the respective training signal. Following the aforementioned procedure, it is possible to excite all degrees of freedom simultaneously within a single simulation. In this work, however, each modal deflection is computed within a separate unsteady CFD run in order to exploit the parallel computing resources. As a result of each unsteady CFD computation, a time-series of the integral forces as well as the surface pressure coefficients is obtained. If field or surface information with respect to the flow quantities have to be taken into account, the POD-based ROM approach [2] should be considered. Therefore, the snapshot matrix $\mathbf{Y}$ has to be constructed on the basis of the available unsteady training data. Consequently, the POD modes and the associated POD coefficient time series are obtained.

Combining the input signals with the CFD response, the merged input/output dataset is used to calibrate the neuro-fuzzy model in order to realize a nonlinear identification. In case of the ROM robust to varying freestream conditions [1], the integral forces (aerodynamic coefficients or generalized aerodynamic forces) at several static flow conditions are used for model training, while the static input parameter θ introduced in Eq. 4 is taken into consideration. For the POD-ROM approach [2], in contrast, the transient POD coefficients serve as the model output. As the ROM proposed in [2] is formulated for fixed flow conditions, the parameter θ is not included within the model input vector. After arranging the data according to the external dynamics approach, the ROM can be trained via the LOLIMOT algorithm.

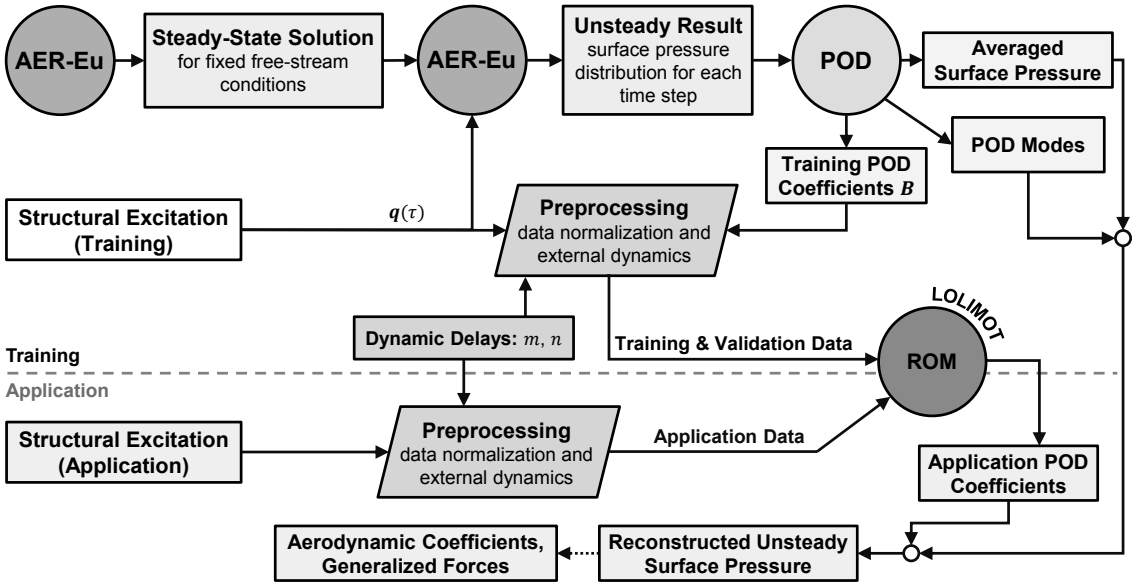

Figure 2: Overview of the aerodynamic ROM involing neuro-fuzzy models and the proper orthogonal decomposition.

Finally, the ROM can be used for time-marching simulations with respect to arbitrary excitation signals. Therefore, the model outputs such as the estimated integral forces or the predicted POD coefficients have to be fed back iteratively to the model input vector for each time step. It is important to emphasize that the discrete time step size embedded in the training data must be respected for all ROM-based simulations. Hence, the obtained integral forces can be used for aeroelastic investigations, whereas the ROM-generated POD coefficients can be employed to reconstruct the unsteady surface pressure distribution caused by the user-defined motion.

4 RESULTS

4.1 Test Case: Common Research Model

The ROM approaches recapitulated in the previous section are demonstrated based on the CRM configuration [27,28], which has been developed by NASA's subsonic fixed wing aerodynamics technical working group in collaboration with the drag prediction workshop (DPW) organizing committee. The CRM variant investigated here is the wing/body/horizontal-tail (WBH) configuration with supercritical wing design that has been in the focus during the 4th AIAA CFD DPW [37]. The configuration is based on a transonic commercial transport aircraft with a cruise Mach number of $Ma_\infty = 0.85$ and a design lift coefficient of $c_L = 0.5$. Important geometrical properties of the CRM configuration are listed in Table 1.

Reference area	A_{ref}	$383.69\ m^2$
Wing span	b	$58.763\ m$
Wing reference chord	c_{ref}	$7.0053\ m$
Aspect ratio	AR	9.0
Quarter chord sweep angle	$\varphi_{1/4}$	$35°$
Taper ratio	λ	0.275

Table 1: Geometric properties of the CRM configuration.

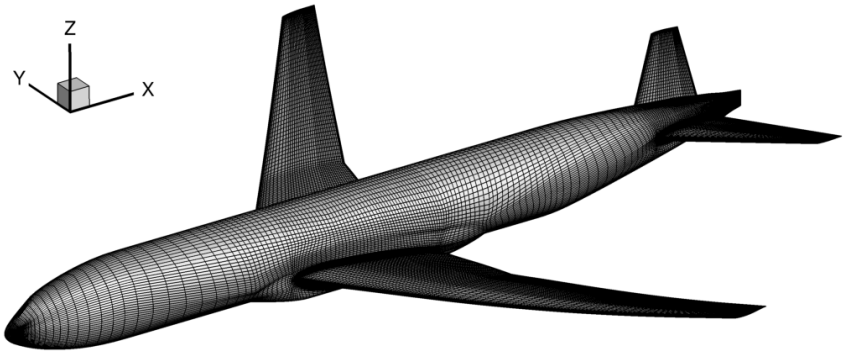

Figure 3: Structured surface grid of the CRM configuration involving 67856 surface elements.

In contrast to the half-model considered within the DPW 4, the full aircraft is investigated here to enable time-marching aerodynamic simulations of symmetric as well as antisymmetric motions. For ensuring the independence of the solution from the mesh resolution, a grid sensitivity study has been conducted yielding a block-structured grid containing 5,864,752 finite volume cells. In Fig. 3, the surface discretization of the CRM configuration is shown. With respect to the structural modeling, the FERMAT configuration introduced by Klimmek [29] is utilized. This finite element model has been developed to obtain a generic aircraft test case on the basis of the CRM geometry. However, as the vertical stabilizer, the pylon, and the engines included in the FERMAT model are not part of the underlying aerodynamic model, the associated structural elements have been also neglected within the FE model for the present purposes. Here, the elastic mode shapes represented by FERMAT mass case C2 (maximum take-off weight with 100% fuel) are adopted for conducting the forced-motion aerodynamic simulations.

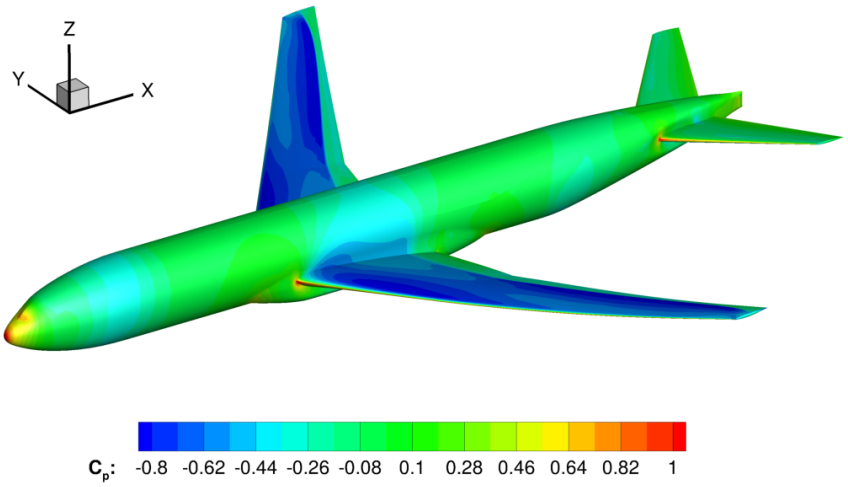

Figure 4: Steady-state pressure coefficient distribution for the CRM configuration at $Ma_\infty = 0.85$ and $c_L = 0.5$ (AER-Eu).

In the course of this investigation, neither static aeroelastic deformation nor trimming is taken into account. Hence, a generic test case incorporating increased geometric complexity is obtained, whereas the modeling strategy is kept as simple as possible. It should be emphasized that the aim followed here is not the comparison between different CFD solvers, aeroelastic modeling approaches, or a fit evaluation exploiting experimental data but to provide a clean ROM testing framework. Nonetheless, all challenging aspects regarding a ROM performance assessment are included, e.g., the presence of realistic structural eigenmodes as well as an overall

complex geometry, the necessity to model a wide excitation frequency bandwidth, the consideration of both symmetric and antisymmetric motions, and the ability to capture aerodynamic nonlinearities caused by strong shocks along the wingspan (see Fig. 4 for instance).

Elastic mode 1, $f = 1.0574\ Hz$ | Elastic mode 2, $f = 1.4547\ Hz$

Elastic mode 11, $f = 3.6033\ Hz$ | Elastic mode 24, $f = 10.6024\ Hz$

Figure 5: Surface deformation based on selected structural eigenmodes of the FERMAT configuration [29]. For a clearer presentation, the deflections have been exaggerated.

Given the baseline CFD grid of the CRM model and the FERMAT database, the interpolation of the elastic-mode-shape-based deflections onto the surface grid has been achieved via the thin-plate spline (TPS) method. Four deformed surface grids are depicted exemplarily in Fig. 5. In contrast to the visualized deflections, however, the actually considered deformations have been scaled to maximum amplitudes of $A_{max} = 0.1\%\ c_{ref}$. In this way, dynamic linearity around the (nonlinear) reference state is ascertained. However, nonlinear ROM techniques are required due to freestream condition variations [1] or the application of the POD procedure [2].

4.2 ROM Application Across Angle of Attack Variations

According to the ROM process outlined in Fig. 1, steady CFD simulations corresponding to the training freestream conditions have been conducted. Here, the freestream Mach number is considered fixed at $Ma_\infty = 0.85$, while angles of attack of $\alpha_{Trn} = [0.5°, 1.0°, 1.5°, 2.0°]$ are taken into account for the training dataset. Subsequently, the aerodynamic responses due to forced mode-shape-based excitations have been computed by means of the AER-Eu solver for all freestream conditions as well as elastic eigenmodes. Therefore, an amplitude-modulated pseudo-random binary signal (APRBS, [1, 35]), which has been a posteriori smoothed, is utilized as the training excitation signal; see Fig. 6. Based on the pre-defined discrete time step size of $\Delta\tau = 0.05$ and the smoothed APRBS depicted in Fig. 6, 1200 training samples of the aerodynamic response in terms of $\mathbf{f}_{gen}$ are obtained for each combination of α_{Trn} and q_i. Following the nonlinear identification procedure, the LOLIMOT algorithm has been applied to obtain the ROM on the basis of the available training data. Thereby, the dynamic delay orders are optimized to be $m = 8$ and $n = 3$ for the respective inputs q_i and GAF outputs $\mathbf{f}_{gen}$ according to the procedure discussed in [2].

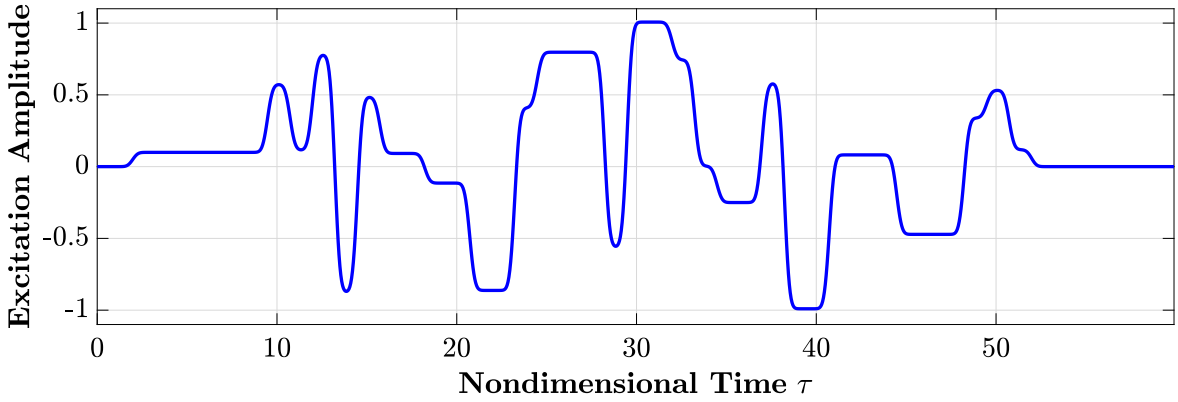

Figure 6: Smoothed APRBS time series for the forced-motion excitation of the structural degrees of freedom (number of training samples: 1200, $\Delta\tau = 0.05$).

Finally, the trained ROM can be used to simulate the time-domain aerodynamic response at a range of freestream conditions. In [1] it has been shown that the **GAF** matrix known from classical stability analysis can be constructed by applying harmonic excitations in each generalized coordinate. Within this study, the freestream condition characterized by $Ma_\infty = 0.85$ and $\alpha_{Sim} = 1.13°$ (corresponding to the design lift coefficient $c_L = 0.5$ for the underlying Euler-equation solution) is set into focus. This angle of attack was not explicitly included in the training dataset. Here, various reduced frequencies $k_{red,ROM} = [0.1, 0.2, 0.5, 1.0, 2.0, 3.0, 4.0, 5.0]$ have been simulated with the ROM. In contrast, the CFD reference solution was computed for the following reduced frequencies: $k_{red,CFD} = [0.1, 0.2, 0.5, 1.0, 2.0, 5.0]$. In order to neglect the initial transient response, three oscillation cycles are simulated with the ROM as well as the AER-Eu solver. Subsequently, the obtained time-domain responses can be transferred into the frequency domain by means of a Fourier analysis with respect to the third excitation cycle. The complex valued **GAF** matrix resulting from this procedure is visualized for selected excitation and generalization degrees of freedom in Fig. 7 as a function of the reduced frequency. In this regard, the real part is denoted by Re, whereas the imaginary part is symbolized by Im. As it can be seen from Fig. 7, generally a very good agreement is ascertained for the present case. This applies, especially, to the diagonal of the GAF matrix. Except from some discrepancies at low excitation frequencies (see the imaginary part of $GAF_{24,11}$ or $GAF_{24,19}$ for instance), a high accuracy is achieved using the ROM-based modeling. The present errors can be traced back to the training signal, which does not optimally excite the lower frequency band. Nonetheless, the results demonstrate that this ROM approach [1] can yield very promising results even for full-size aircraft configurations involving realistic structural eigenmodes.

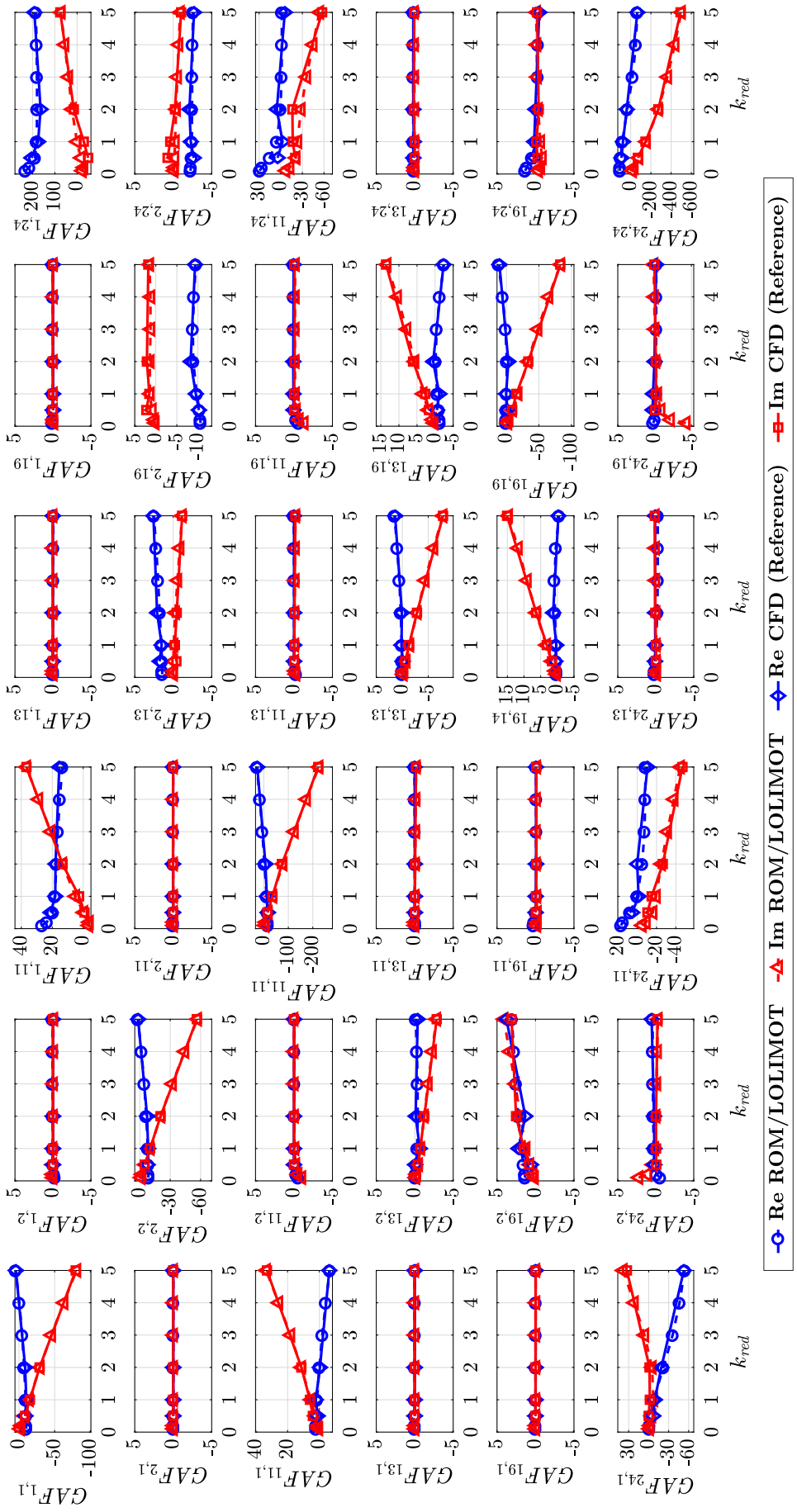

Figure 7: Real and imaginary parts of the frequency-domain GAF matrix computed by the ROM [1] as well as the AER-Eu solver ($Ma_\infty = 0.85$, $\alpha_{Sim} = 1.13°$, CRM configuration, FERMAT structural model).

4.3 ROM Application for Modeling Surface Pressure Distributions

In contrast to the workflow followed in the previous subsection, a single freestream condition ($Ma_\infty = 0.85$, $\alpha_{Sim} = 1.13°$) is considered here for the application of the POD-based ROM procedure [2]; see also Fig. 2. Therefore, the unsteady forced-motion AER-Eu simulations have been performed for all excitation degrees of freedom q_i $(i = 1, \ldots, N)$ at $\alpha_{Sim} = 1.13°$ utilizing the smoothed APRBS visualized in Fig. 6. Again, a nondimensional time step size of $\Delta\tau = 0.05$ has been employed. Exploiting the surface pressure data (1200 samples $\times$ 67856 surface elements) obtained for each of the N unsteady CFD simulations, the POD procedure was executed yielding the POD modes and the associated POD coefficients. In Fig. 8, a selected number of POD modes originating from the unsteady c_p surface distribution is shown. Depending on the excited structural mode shape, between 34 and 42 POD modes were found to be sufficient for the approximation of the training data, i.e., yielding a $RIC > 0.95$. Subsequently, a LOLIMOT-algorithm-based identification with respect to the POD coefficients was carried out, while the dynamic delay orders were set to $m = 25$ and $n = 10$; cf. to the method in [2].

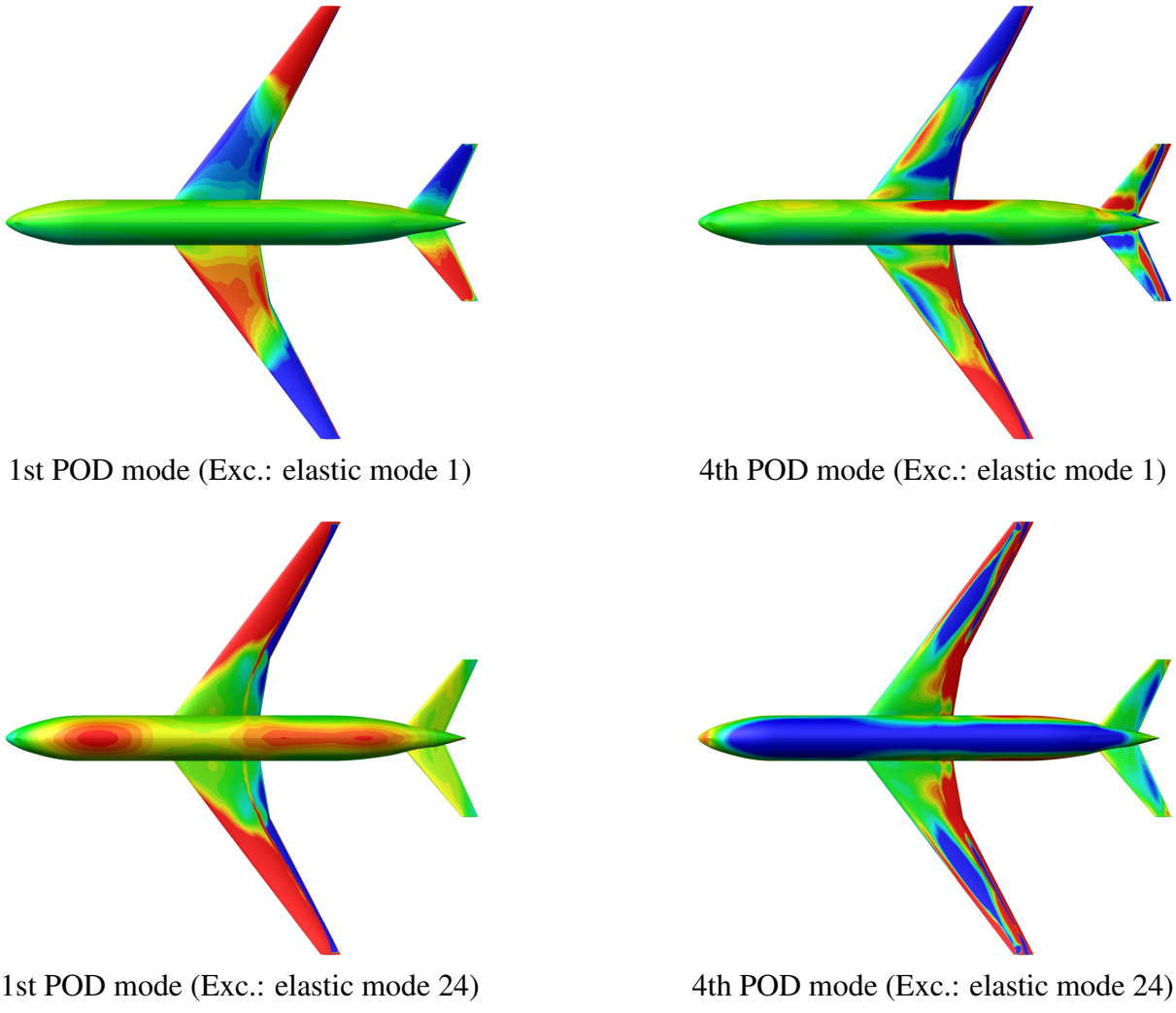

Figure 8: Visualization of selected POD modes which have been extracted from forced-motion unsteady CFD simulations. The excitation (exc.) degree of freedom for the corresponding POD mode set is specified within the parenthesis.

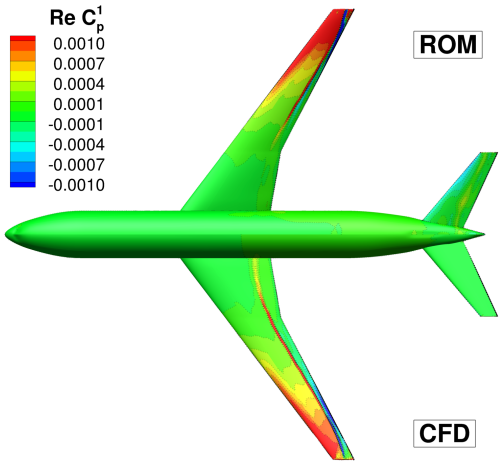

Harmonic exc.: Mode 1, $k_{red} = 0.1$

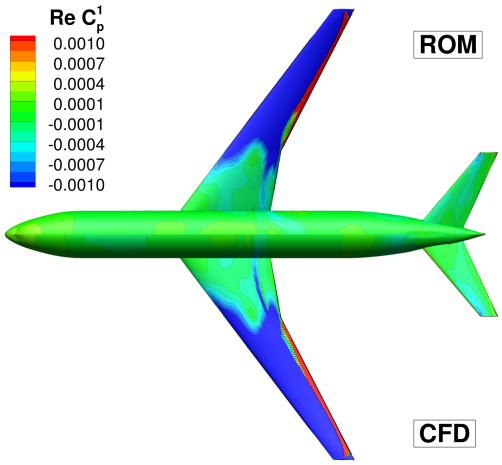

Harmonic exc.: Mode 24, $k_{red} = 1.0$

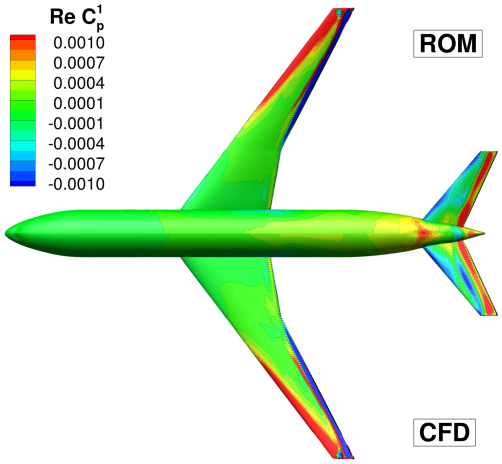

Harmonic exc.: Mode 1, $k_{red} = 5.0$

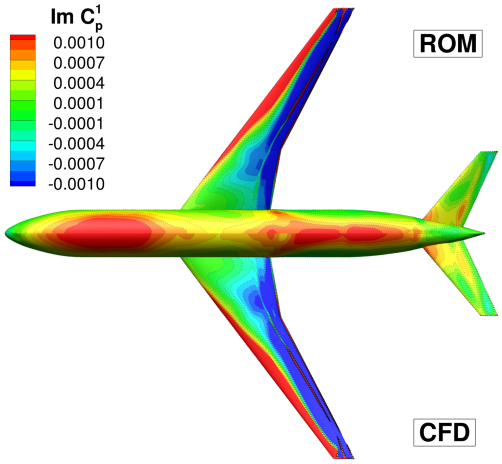

Harmonic exc.: Mode 24, $k_{red} = 5.0$

Figure 9: First harmonic of the pressure coefficient response (upper surface). Due to the symmetric response for symmetric-eigenmode-based excitations, only the half-model results are shown. The ROM result is shown for $y > 0$, whereas the reference result is depicted for $y < 0$. $Ma_\infty = 0.85$, $\alpha = 1.13°$, CRM configuration, FERMAT structural model.

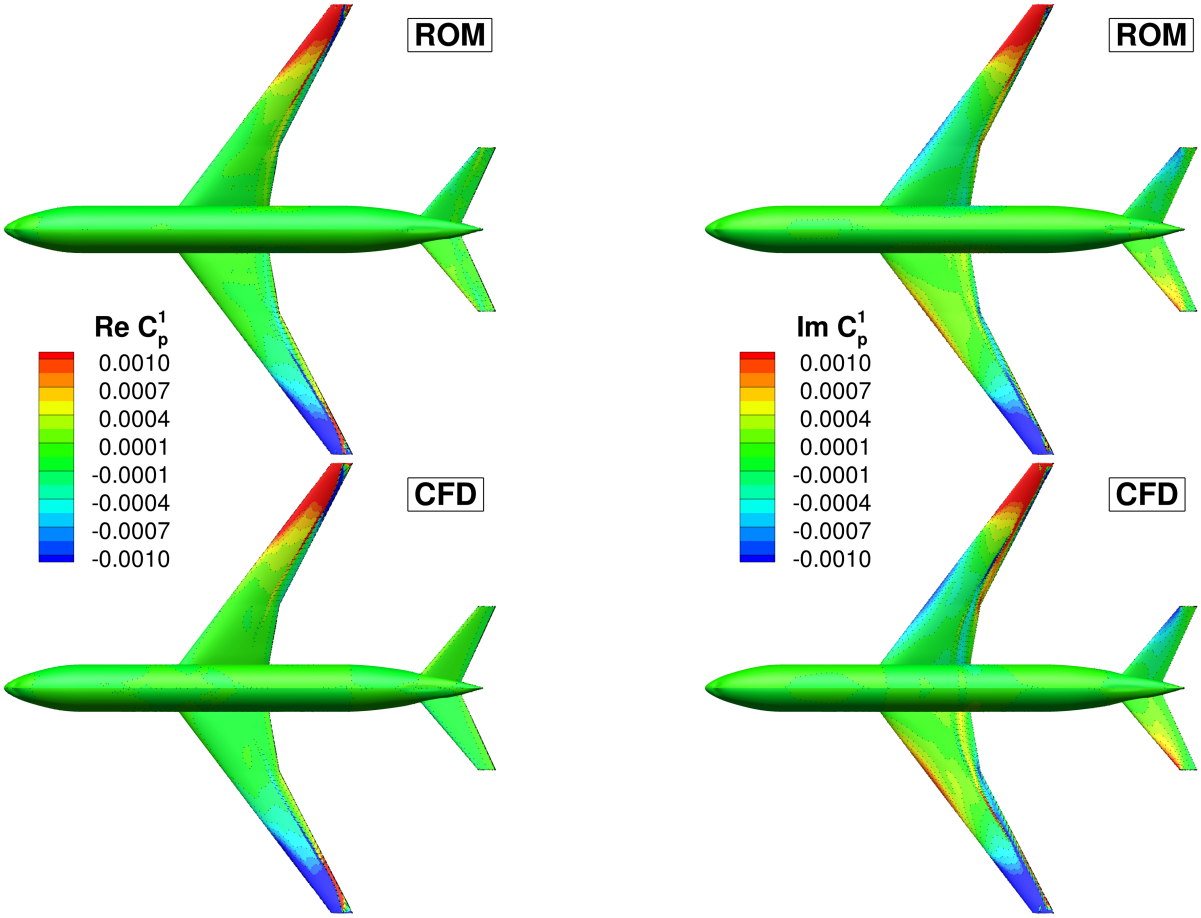

Harmonic exc.: Mode 2, $k_{red} = 0.5$ Harmonic exc.: Mode 2, $k_{red} = 5.0$

Figure 10: First harmonic of the pressure coefficient response (upper surface). Due to the antisymmetric-eigenmode-based excitations, the full configuration is shown. The ROM result is shown at the top, whereas the reference result is depicted at the bottom. $Ma_\infty = 0.85$, $\alpha = 1.13°$, CRM configuration, FERMAT structural model.

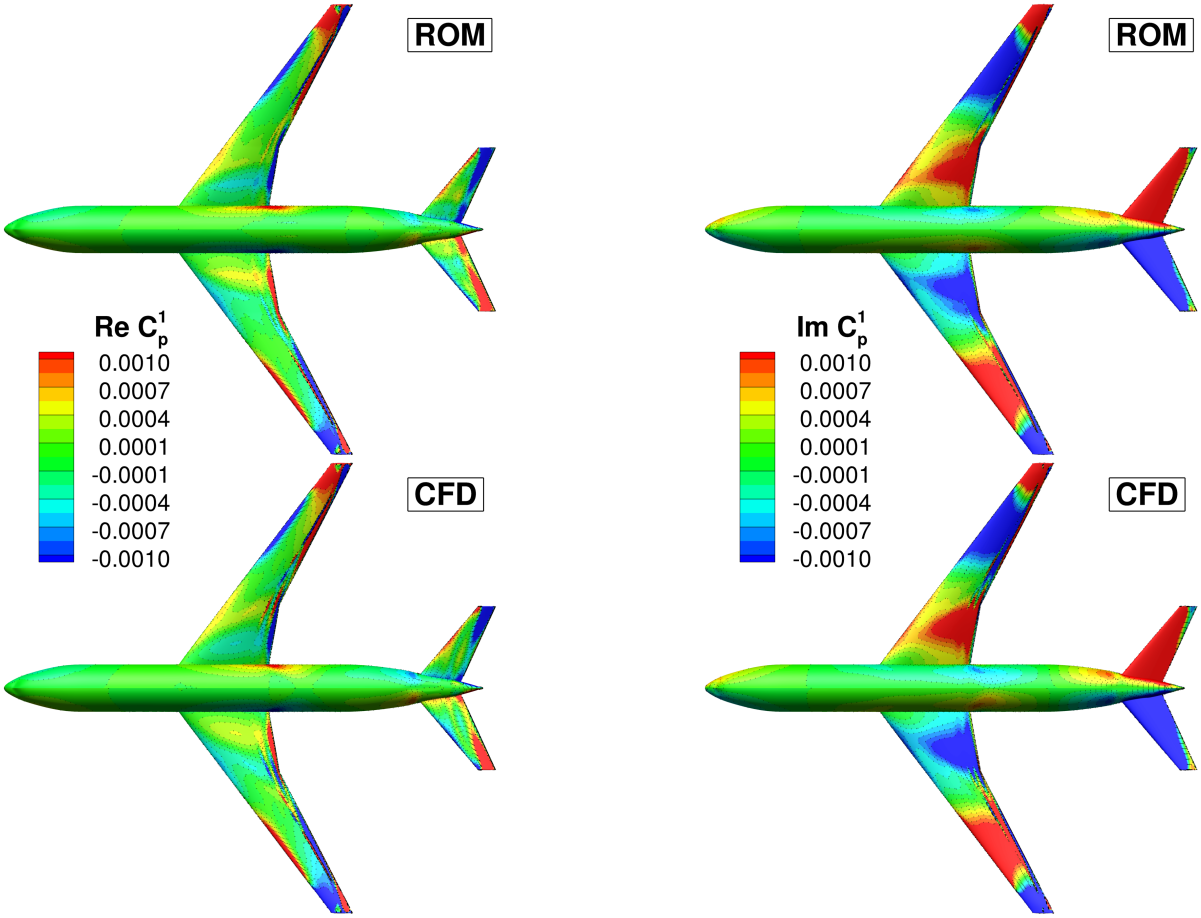

Harmonic exc.: Mode 12, $k_{red} = 5.0$ Harmonic exc.: Mode 12, $k_{red} = 5.0$

Figure 11: First harmonic of the pressure coefficient response visualized for the upper surface. Due to the antisymmetric-eigenmode-based excitations, the full configuration is shown. The ROM result is shown at the top, whereas the reference result is depicted at the bottom. $Ma_\infty = 0.85$, $\alpha = 1.13°$, CRM configuration, FERMAT structural model.

After finishing the POD-ROM training process, the obtained model can be utilized to conduct quasi-steady or unsteady simulations [2]. In the course of this investigation, again harmonic motions characterized by several reduced frequencies $k_{red,ROM} = [0.1, 0.2, 0.5, 1.0, 2.0, 5.0]$ are simulated with respect to the excitation of the generalized coordinates. Therefore, three oscillation cycles have been computed with the POD-based ROM as well as the CFD solver. For a more compact representation, a Fourier analysis with respect to the third excitation cycle was performed to yield the real and imaginary part of the first harmonic surface pressure distribution. However, the time-domain information is available and can be analyzed as well. Moreover, also integral quantities can be computed a posteriori based on the surface information. In Fig. 9, the surface c_p response caused by the excitation of selected symmetric eigenmodes is visualized. The contour plots exhibit a generally good agreement between the ROM and the reference, although the influence of the shock can not be represented accurately by the ROM. This becomes obvious especially in the region of the wing root and has been already noted for the LANN wing [2]. Beside small-scale topological mismatches, the overall flow characteristics are in good accordance. As already discussed in the previous subsection, the ROM performance at lower k_{red} is not as good as for larger reduced frequencies due to the non-optimal training signal design. Furthermore, also the aerodynamic response induced by antisymmetric excitations can be reproduced with sufficient accuracy as can be seen from Figs. 10-11. It can be concluded that the ROM approach [2] can be equivalently applied towards more complex configurations. However, due to the increased size of the problem, the data handling as well as the data input/output can be cumbersome and may exceed the memory/computing limits. The achievable speed-up and the applicability of the method, however, is generally not restricted by the complexity of the test case.

5 CONCLUSIONS

In this paper, two recently developed nonlinear ROM approaches have been applied to assess their performance for unsteady aerodynamic computations. For this purpose, the CRM configuration combined with the FERMAT structural model was investigated in order to study the ROM's characteristics with respect to geometrically more complex test cases. First, a neurofuzzy-model-based ROM was employed to compute harmonic aerodynamic responses due to structural-eigenmode-based excitations across variable angles of attack. It was demonstrated that the approach yielded very promising results along with a speed-up of about 2-3 orders of magnitude compared to the fully CFD-based process, depending on the intended number of computations. Second, the unsteady surface pressure distribution was predicted by a POD-based ROM approach. Thereby, it was shown that the ROM reliably predicts the dominant unsteady pressure field topologies, although the resolution of small-scale structures requires further attention. Nonetheless, the potential of the ROMs towards the application on industry-relevant configurations was indicated.

6 REFERENCES

[1] Winter, M. and Breitsamter, C. (2016). Neurofuzzy-model-based unsteady aerodynamic computations across varying freestream conditions. *AIAA Journal*, 54(9), 2705–2720. doi:10.2514/1.J054892.

[2] Winter, M. and Breitsamter, C. (2016). Efficient unsteady aerodynamic loads prediction based on nonlinear system identification and proper orthogonal decomposition. *Journal of Fluids and Structures*, 67, 1–21. doi:10.1016/j.jfluidstructs.2016.08.009.

[3] Dowell, E. H. and Hall, K. C. (2001). Modeling of fluid-structure interaction. *Annual Review of Fluid Mechanics*, 33(1), 445–490. doi:10.1146/annurev.fluid.33.1.445.

[4] Lucia, D. J., Beran, P. S., and Silva, W. A. (2004). Reduced-order modeling: New approaches for computational physics. *Progress in Aerospace Sciences*, 40(1-2), 51–117. doi:10.1016/j.paerosci.2003.12.001.

[5] Silva, W. A. (1997). *Discrete-Time Linear and Nonlinear Aerodynamic Impulse Responses for Efficient CFD Analyses: Ph.D. Dissertation*. Williamsburg, VA: College of William and Mary.

[6] Raveh, D. E. (2001). Reduced-order models for nonlinear unsteady aerodynamics. *AIAA Journal*, 39(8), 1417–1429. doi:10.2514/2.1473.

[7] Hall, K. C., Thomas, J. P., and Dowell, E. H. (2000). Proper orthogonal decomposition technique for transonic unsteady aerodynamic flows. *AIAA Journal*, 38(10), 1853–1862. doi:10.2514/2.867.

[8] Iuliano, E. and Quagliarella, D. (2013). Proper orthogonal decomposition, surrogate modelling and evolutionary optimization in aerodynamic design. *Computers & Fluids*, 84, 327–350. doi:10.1016/j.compfluid.2013.06.007.

[9] Silva, W. A. and Bartels, R. E. (2004). Development of reduced-order models for aeroelastic analysis and flutter prediction using the CFL3Dv6.0 code. *Journal of Fluids and Structures*, 19(6), 729–745. doi:doi:10.1016/j.jfluidstructs.2004.03.004.

[10] Silva, W. A. (2008). Simultaneous excitation of multiple-input/multiple-output CFD-based unsteady aerodynamic systems. *Journal of Aircraft*, 45(4), 1267–1274. doi:10.2514/1.34328.

[11] Fleischer, D. and Breitsamter, C. (2013). Efficient computation of unsteady aerodynamic loads using computational-fluid-dynamics linearized methods. *Journal of Aircraft*, 50(2), 425–440. doi:10.2514/1.C031851.

[12] Winter, M., Heckmeier, F. M., and Breitsamter, C. (2017). CFD-based aeroelastic reduced-order modeling robust to structural parameter variations. *Aerospace Science and Technology*, 67, 13–30. doi:10.1016/j.ast.2017.03.030.

[13] Raveh, D. E. (2004). Identification of computational-fluid-dynamics based unsteady aerodynamic models for aeroelastic analysis. *Journal of Aircraft*, 41(3), 620–632. doi:10.2514/1.3149.

[14] Faller, W. E. and Schreck, S. J. (1997). Unsteady fluid mechanics applications of neural networks. *Journal of Aircraft*, 34(1), 48–55. doi:10.2514/2.2134.

[15] Voitcu, O. and Wong, Y. S. (2003). Neural network approach for nonlinear aeroelastic analysis. *Journal of Guidance, Control, and Dynamics*, 26(1), 99–105. doi:10.2514/2.5019.

[16] Mannarino, A. and Mantegazza, P. (2014). Nonlinear aeroelastic reduced order modeling by recurrent neural networks. *Journal of Fluids and Structures*, 48, 103–121. doi:10.1016/j.jfluidstructs.2014.02.016.

[17] Zhang, W., Wang, B., Ye, Z., et al. (2012). Efficient method for limit cycle flutter analysis based on nonlinear aerodynamic reduced-order models. *AIAA Journal*, 50(5), 1019–1028. doi:10.2514/1.J050581.

[18] Winter, M. and Breitsamter, C. (2014). Reduced-order modeling of unsteady aerodynamic loads using radial basis function neural networks. In *63rd Deutscher Luft- und Raumfahrtkongress, Augsburg, Germany, Deutsche Gesellschaft für Luft- und Raumfahrt Paper 2014-340013*. pp. 1–10.

[19] Kou, J., Zhang, W., and Yin, M. (2016). Novel wiener models with a time-delayed nonlinear block and their identification. *Nonlinear Dynamics*, 85(4), 2389–2405. doi: 10.1016/j.jfluidstructs.2016.10.011.

[20] Kou, J. and Zhang, W. (2017). Layered reduced-order models for nonlinear aerodynamics and aeroelasticity. *Journal of Fluids and Structures*, 68, 174–193. doi: 10.1016/j.jfluidstructs.2016.10.011.

[21] Park, S., Jun, K., Baek, S., et al. (2013). Reduced-order model with an artificial neural network for aerostructural design optimization. *Journal of Aircraft*, 50(4), 1106–1116. doi:10.2514/1.C032062.

[22] Lindhorst, K., Haupt, M., and Horst, P. (2014). Efficient surrogate modelling of nonlinear aerodynamics in aerostructural coupling schemes. *AIAA Journal*, 52(9), 1952–1966. doi: 10.2514/1.J052725.

[23] Lindhorst, K., Haupt, M., and Horst, P. (2015). Aeroelastic analyses of the high-reynolds-number-aerostructural-dynamics configuration using a nonlinear surrogate model approach. *AIAA Journal*, 53(9), 2784–2796. doi:10.2514/1.J053743.

[24] Glaz, B., Liu, L., and Friedmann, P. P. (2010). Unsteady aerodynamic modeling using a surrogate-based recurrence framework. *AIAA Journal*, 48(10), 2418–2429. doi: 10.2514/1.J050471.

[25] Liu, H., Hu, H., Zhao, Y., et al. (2014). Efficient reduced-order modeling of unsteady aerodynamics robust to flight parameter variations. *Aerospace Science and Technology*, 49, 728–741. doi:10.1016/j.jfluidstructs.2014.06.015.

[26] Winter, M. and Breitsamter, C. (2016). Sensitivity analysis of unsteady aerodynamic reduced-order models robust to freestream parameter variations. In *30th Congress of the International Council of the Aeronautical Sciences, Daejeon, Korea*. pp. 1–11.

[27] Vassberg, J., Dehaan, M., Rivers, M., et al. (2008). Development of a common research model for applied cfd validation studies. In *26th AIAA Applied Aerodynamics Conference. Honolulu, Hawaii*. pp. 1–22.

[28] Rivers, M. and Dittberner, A. (2010). Experimental investigations of the nasa common research model. In *28th AIAA Applied Aerodynamics Conference. Chicago, Illinois*. pp. 1–35.

[29] Klimmek, T. (2014). Parametric set-up of a structural model for FERMAT configuration aeroelastic and loads analysis. *Journal of Aeroelasticity and Structural Dynamics*, 3(2), 31–49. doi:10.3293/asdj.2014.27.

[30] Wright, J. R. and Cooper, J. E. (2007). *Introduction to Aircraft Aeroelasticity and Loads*. West Sussex, England, U.K.: Wiley & Sons.

[31] Kreiselmaier, E. and Laschka, B. (2000). Small disturbance Euler equations: Efficient and accurate tool for unsteady load prediction. *Journal of Aircraft*, 37(5), 770–778. doi: 10.2514/2.2699.

[32] Pechloff, A. and Laschka, B. (2006). Small disturbance Navier-Stokes method: Efficient tool for predicting unsteady air loads. *Journal of Aircraft*, 43(1), 17–29. doi: 10.2514/1.14350.

[33] Pechloff, A. and Laschka, B. (2010). Small disturbance Navier-Stokes computations for low-aspect-ratio wing pitching oscillations. *Journal of Aircraft*, 47(3), 737–753. doi: 10.2514/1.45233.

[34] Förster, M. and Breitsamter, C. (2015). Aeroelastic prediction of discrete gust loads using nonlinear and time-linearized CFD-methods. *International Journal of Aeroelasticity and Structural Dynamics*, 3(3), 19–38. doi:10.3293/asdj.2015.27.

[35] Nelles, O. (2001). *Nonlinear System Identification: From Classical Approaches to Neural Networks and Fuzzy Models*. Berlin, Germany: Springer-Verlag.

[36] Sirovich, L. (1987). Turbulence and the dynamics of coherent structures. Part 1: coherent structures. *Quarterly of Applied Mathematics*, 45(3), 561–571.

[37] Vassberg, J. C., Tinoco, E. N., Mani, M., et al. (2014). Summary of the fourth aiaa computational fluid dynamics drag prediction workshop. *Journal of Aircraft*, 51(4), 1070–1089. doi:10.2514/1.C032418.

COPYRIGHT STATEMENT